

Correlated states in charge-transfer heterostructures based on rhombohedral multilayer graphene

Yanran Shi,¹ Min Li,¹ Xin Lu,^{1,*} and Jianpeng Liu^{1,2,†}

¹*School of Physical Science and Technology, ShanghaiTech Laboratory for Topological Physics, State Key Laboratory of Quantum Functional Materials, ShanghaiTech University, Shanghai 201210, China*

²*Liaoning Academy of Materials, Shenyang 110167, China*

Charge transfer is a common phenomenon in van der Waals heterostructures with proper work function mismatch, which enables electrostatic gating to control band alignment and interlayer charge distributions. This provides a tunable platform for studying coupled bilayer correlated electronic systems. Here, we theoretically investigate heterostructures of rhombohedral multilayer graphene (RMG) and an insulating substrate with gate-tunable band alignment. We first develop a self-consistent electrostatic theory for layer charge densities incorporating charge transfer, which reproduces the experimentally observed broadened and bent charge neutrality region. When the substrate's band edge has a much larger effective mass than RMG, its carriers can form a Wigner crystal at low densities. This creates a quantum superlattice that induces topological flat bands in the RMG layer, which may lead to Chern insulators driven by intralayer Coulomb interactions. Conversely, with comparable effective masses, we find an interlayer excitonic insulator state at charge neutrality stabilized by interlayer Coulomb coupling. Our work establishes these charge-transfer heterostructures as a rich platform for topological and excitonic correlated states, opening an avenue for “charge-transferonics”.

Two-dimensional (2D) van der Waals heterostructures [1], assembled by stacking chemically distinct atomically thin layers in a designed sequence, provide a highly tunable platform for emergent quantum phenomena including topological insulators, magnetic skyrmion textures and fractional Chern insulators [2–19]. A key ingredient underlying the rich physics is the ability to control the electronic structure *in situ* with electrostatic gates. If the band edges of the two constituent layers have overlap, electrons would tunnel from an occupied band in one layer into an empty band in the other, which defines a charge-transfer heterostructure. Interlayer Coulomb interactions can then generate synergistic correlated phases that cannot be realized in isolated individual layers [20, 21]. This gate-controlled interlayer charge transfer in 2D van der Waals heterostructures thus opens an avenue for “charge-transferonics”, i.e., engineering novel electronic phases and functionality based on charge-transfer mechanisms [20–23].

A promising realization is provided by stacking graphene multilayers on insulating substrates with proper work function mismatch. Assisted by electrostatic gating, the low-energy bands of graphene can be aligned with the band edges of the substrate, offering a fertile playground for studying the interplay of strong correlations and band topology. As schematically illustrated in the upper panel of Fig. 1(a), when the charge density induced in the substrate remains below a critical threshold, the transferred electrons can form a Wigner crystal at the interface driven by Coulomb interactions [24]. This interfacial charge order generates a long-wavelength superlattice potential that acts on graphene via interlayer Coulomb interactions and narrows the subband band-

width, thereby enhancing electronic correlations, in close analogy to the scenario of moiré materials [25, 26]. Indeed, charge-transfer-driven correlated states have been experimentally realized in a series of graphene-insulator heterostructures. These states manifest as unusually robust quantum Hall states in monolayer graphene-CrOCl [21], unconventional correlated insulating state in bilayer graphene (BLG)-CrOCl [22], and analogous phenomena in other graphene-based heterostructures [27–29].

Compared with monolayer graphene, RMG hosts low-energy bands that are flattened by interlayer hopping and can carry substantial Berry curvature, thereby enhancing interaction effects and facilitating the emergence of topological correlated states [2, 30–44]. It is therefore natural to expect that even more exotic correlated phases may arise in RMG-insulator charge-transfer heterostructures. In this work, we theoretically investigate charge-transfer heterostructures of rhombohedral multilayer graphene (RMG) on insulating substrates under realistic conditions. We develop a self-consistent electrostatic screening theory that quantitatively reproduces the puzzling experimentally observed bent and broadened charge neutrality region [22]. First, separating the electronic degrees of freedom of the two layers [20], we find that a sufficiently heavy substrate band edge's mass enables dilute carriers to form a Wigner crystal, which generates superlattice potential exerting on RMG, thus produces topological flat subbands [Fig. 1(b)] [45–50]. In this regime, Chern-insulator phases are found at subband fillings $\nu = 1, 2$ for sufficiently large superlattice period driven by intralayer Coulomb interactions.

Then, treating both layers on equal footing, we find that opposite charge doping at overall neutrality favors

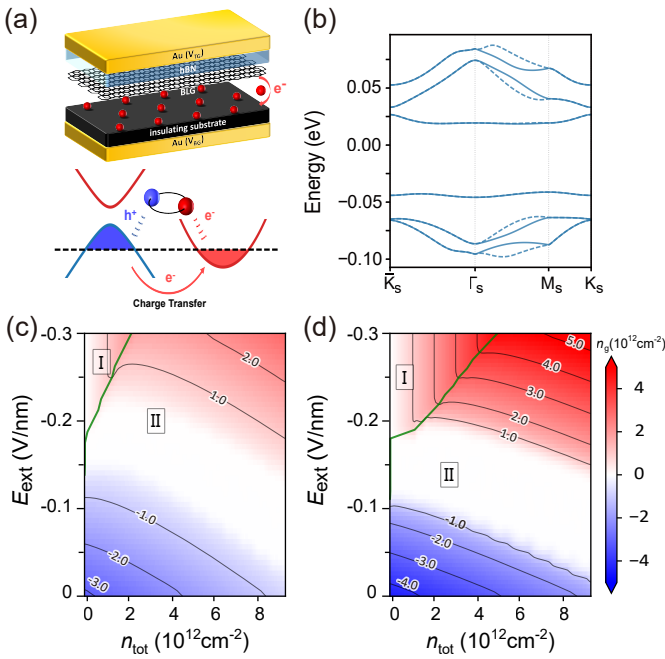


FIG. 1. (a) Upper panel: schematic image of device and the interface electron crystal formed at the surface of substrate. Lower panel: schematic image of an interlayer exciton. (b) Non-interacting energy band of BLG modulated by interlayer superlattice potential. (c,d) Carrier densities of the RMG n_g in a RMG-CrOCl heterostructures given in (c) for BLG-CrOCl and in (d) for TriLG-CrOCl. The black solid lines mark iso-doping levels in RMG.

interlayer electron-hole binding [lower panel of Fig. 1(a)] and stabilizes an interlayer excitonic insulator (IEI) under appropriate conditions. [51–58] With excess charge doping, the substrate develops the same Wigner-crystal-like charge order assumed above, supporting the consistency and physical plausibility of the Wigner-superlattice scenario.

Electrostatic screening model To accurately determine layer charge density distributions for the charge-transfer heterostructures, one needs to carefully treat the screening of vertical electric field E_{ext} applied to the system. We start with the non-interacting Hamiltonian $H^0 = H_{\text{RMG}}^0 + H_{\text{sub}}^0$, where H_{RMG}^0 is the non-interacting $\mathbf{k} \cdot \mathbf{p}$ model of RMG [59]; and H_{sub}^0 is the non-interacting continuum model of the carriers transferred to the substrate, which is assumed to take the form of 2D electron gas characterized by effective mass m^* [59]. Without loss of generality, we suppose the carriers are transferred to the conduction band minimum (CBM) of the substrate, which has a relative energy shift E_{CBM} with respect to the CNP of RMG. The interlayer hopping between RMG and the substrate is typically negligible, as confirmed by density functional theory (DFT) calculations [21], because the interlayer hopping is exponentially suppressed due to the large interlayer distance and lattice mismatch

in such heterostructures. This endows an emergent layer $U(1)$ symmetry for the low-energy electrons in such system, the spontaneous breaking of which gives rise to an IEI, as will be discussed later.

Under E_{ext} , diagonalizing the above Hamiltonian yields the charge distributions at different layers of the RMG-substrate heterostructure. The redistributed charges, however, modify the interlayer electrostatic potential differences through two distinct and competing mechanisms: one from conventional dielectric screening, and the other from the modification of E_{CBM} due to Fock self energy correction. To capture both effects, we formulate a self-consistent screening model incorporating the Fock correction δE_{CBM} alongside conventional dielectric screening effects. Specifically, we first calculate the layer-resolved charge densities using the above non-interacting Hamiltonian, which serves as the source term in the Poisson equation of electrostatic potential. Meanwhile, the Fock correction δE_{CBM} is added to the on-site energy of the substrate. The updated electrostatic potential is fed back into the Hamiltonian to further calculate layer charge density. This calculation is iterated until both the layer charge density and the electrostatic potential converge. More details are given in Supplemental Materials [59].

We illustrate our electrostatic screening model using a heterostructure consisted of RMG and CrOCl. The CBM of CrOCl is mostly contributed by Cr's 3d orbitals, which thus has a large effective mass $m^* \approx 1.3m_0$ [20, 21] (m_0 is bare electron mass). We take $E_{\text{CBM}} = -0.13\text{eV}$ with respect to the Dirac point of graphene, as extracted from DFT calculations [21]. It is worth noting that different choices of m^* and antiferromagnetic configurations of CrOCl do not change the qualitative conclusions presented in this work as magnetic exchange coupling between CrOCl and RMG is negligibly weak [21, 28]. Fig. 1(c,d) present the carrier density of RMG n_g in the parameter space spanned by E_{ext} and the total carrier density n_{tot} , for BLG-CrOCl [Fig. 1(c)], trilayer graphene (TriLG)-CrOCl [Fig. 1(d)], respectively. These phase diagrams exhibit a common feature: upon tuning E_{ext} and n_{tot} , the graphene system evolves from a conventional region (Region I), in which the substrate remains undoped, to a region with significant charge transfer across the interface (Region II). Within Region II, increasing the amplitude of E_{ext} drives RMG continuously from hole-doped state (blue), through the broad CNP region (white), to electron-doped state (red). The iso-density levels in RMG, shown as black curves, exhibit sharp turning points, highlighting the intriguing nonlinear dependence of the equilibrium carrier density on both E_{ext} and n_{tot} due to charge transfer.

Notably, our calculations successfully reproduce the pronounced “broad” and “bent” CNP region of RMG that has been observed in previous transport measurements of BLG-CrOCl devices [22]. These characteristic

features of RMG charge-transfer heterostructure are attributed to the competition between two different mechanisms. On one hand, the screening from re-distribution of layer charge density would reduce the electric field between the substrate and RMG by $n_{\text{sub}}e^2/(\epsilon_0\epsilon_r)$, which reduces the carrier density transferred to the substrate. On the other hand, the long-range Coulomb interactions among transferred carriers in the substrate generate a negative Fock self-energy δE_{CBM} , which would lower the substrate's CBM by an amount $\frac{e^2}{4\pi\epsilon_0\epsilon_r}\sqrt{2\pi n_{\text{sub}}}$, thus effectively enhancing the interlayer electric field. At low n_{sub} , the Fock correction term, proportional to $\sqrt{n_{\text{sub}}}$, dominates over the dielectric screening effect $\sim n_{\text{sub}}$. This leads to upward-curved iso-doping lines and bent phase boundaries between hole-doped (electron-doped) region and the CNP region. As n_{sub} increases, the linear correction due to the dielectric screening effect dominates, resulting in iso-density lines that drop almost linearly. The significant expansion of the CNP region is also due to such competition [59]. The agreement between our theoretical predictions and experimental observations validates the effectiveness of our modelling for such charge-transfer heterostructure [22, 59].

Chern insulator boosted by Wigner crystallization
The full interacting Hamiltonian of the heterostructure can be decomposed into three parts: the RMG part, the substrate part, and the interlayer Coulomb coupling between them [20]. The large effective mass of the substrate's carriers allows for a “Born-Oppenheimer-type” treatment to the heterostructure, i.e., the ground-state wavefunction is expressed as the product state of that of RMG and that of the substrate [20]. As long as n_{sub} is below a threshold value, the corresponding Wigner-Seitz radius $r_s \gtrsim 31$ [60], a Wigner-crystal-like long-wavelength charge ordered state is expected to form at the surface of the substrate [21]. Such long-wavelength charge order from Wigner crystallization of the substrate's carriers imposes an effective superlattice potential to the electrons in the RMG layer. Thus, we obtain the low-energy effective continuum model for the RMG coupled to insulating substrate [59]

$$\hat{H}_{\text{RMG}}^{0,\mu} = \hat{H}_{\text{RMG}}^{0,\mu} + U_s(\mathbf{r}) + U_d \quad (1)$$

where U_d is the layer-resolved on-site energy obtained from self-consistent electrostatic screening calculation. $U_s(\mathbf{r})$ is the superlattice potential from substrate's long-wavelength charge order with the period $U_s(\mathbf{r}) = U_s(\mathbf{r} + \mathbf{L}_s)$ with \mathbf{L}_s superlattice vector.

Considering the continuum model with renormalized parameters due to the Coulomb potential from high-energy electrons [59, 61–63], we find that for a superlattice period exceeding 10 nm, isolated flat bands appear. The lowest conduction band (LCB) carries a nonzero Chern number ($|C| = 1$) as shown Fig. 1(b) for BLG [59]. We map out the experimentally relevant parameter space (E_{ext}, n_g) in which the LCB of BLG and TriLG exhibit

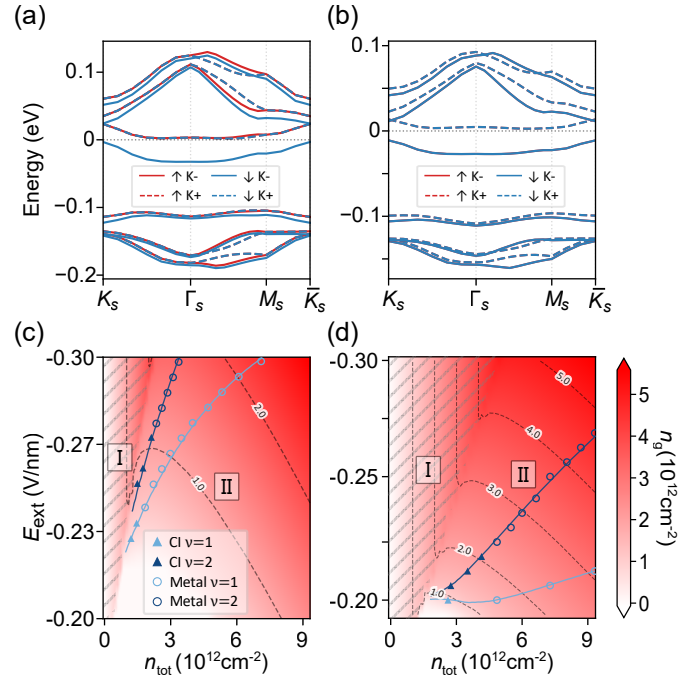


FIG. 2. HF single particle spectra for HF ground state of BLG: (a) at $E_{\text{ext}} = -0.2375 \text{ V/nm}$ and $n_{\text{tot}} = 1.48 \times 10^{12} \text{ cm}^{-2}$ with filling factor $\nu = 1$; and (b) at $E_{\text{ext}} = -0.25 \text{ V/nm}$ and $n_{\text{tot}} = 1.48 \times 10^{12} \text{ cm}^{-2}$ with filling factor $\nu = 2$. The HF ground states along iso-filling lines $\nu = 1$ and $\nu = 2$ are shown in (c) for BLG-CrOCl, and in (d) for TriLG-CrOCl, where color coding represents carrier density n_g of RMG, “CI” denotes Chern insulator state.

a Chern number $|C| = 1$ in Fig. 2(c,d), respectively. The gray shaded area denotes the conventional state without charge transfer, while dashed lines mark iso-density levels in the RMG layer. Solid lines indicate the iso-filling conditions $\nu = 1$ and $\nu = 2$ of the Wigner-crystal supercell ($\nu = \sqrt{3}L_s n_g/2$, assuming a triangular superlattice as expected for a Wigner crystal [24]). These topologically nontrivial flat bands, when filled with electrons, are expected to host novel quantum states [45–50].

To explore the many-body ground state of the RMG, we further study the e - e interaction effects within a band-projected HF approximation [59]. At integer fillings $\nu = 1, 2$, Chern insulator states emerge as HF ground states through spontaneous symmetry breaking, as shown in Fig. 2(a,b) for BLG. While a spin-valley polarized $|C| = 1$ Chern insulator emerges as the ground state for $\nu = 1$, a spin-degenerate but valley-polarized $|C| = 2$ Chern insulator is found for $\nu = 2$. Similar correlated Chern insulators are also identified for TriLG [59]. In Fig. 2(c,d), we present the calculated ground states of RMG along the $\nu = 1$ and $\nu = 2$ iso-filling lines, where open circles denote metallic states and filled triangles indicate Chern insulator. Chern insulator states arise near the charge-transfer phase boundary, where the formed Wigner superlattice exhibits a long period due to

the low transferred carrier density. In this regime, the subbands exhibit narrow bandwidths, leading to the formation of flat bands with nonzero Chern numbers after coupled with Wigner superlattice potential, which subsequently evolve into Chern insulators driven by interactions. Away from the charge-transfer boundary, the superlattice period shortens, resulting in more dispersive subbands that favor a metallic state rather than a gapped insulator.

Interlayer excitonic insulator As discussed above, the full interacting Hamiltonian of the coupled bilayer system possesses an emergent layer $U(1)$ symmetry due to the negligible interlayer hopping. Nevertheless, charge carriers of the two layers are coupled via interlayer Coulomb interactions. If the two layers are oppositely charged, the electron-hole pairs from the two layers may bind together driven by interlayer Coulomb interactions and form a condensate, leading to an excitonic insulator state. Such a state is beyond the “Born-Oppenheimer-type” treatment discussed above. We need to consider the RMG-substrate heterostructure as a unified quantum many-body system. To this end, we adopt a full-band HF method [59] to study the ground state of the heterostructure. Specifically, we treat the effective mass of substrate’s carriers m^* and initial CBM E_{CBM} as two parameters, and vary them to explore the ground-state phase diagram.

Fig. 3(a) presents the phase diagram of the BLG-substrate heterostructure. At large $|E_{\text{CBM}}|$ and small m^*/m_0 , the system favors metallic state, corresponding to the gray region. The inset at the left lower corner in Fig. 3(a) schematically illustrates the band alignment that leads to this metallic state, where the horizontal dotted line marks the Fermi level. While for smaller $|E_{\text{CBM}}|$ and large m^*/m_0 , the substrate’s CBM is pushed above the Fermi level such that charge transfer from BLG to the substrate is suppressed. Hence, the system behaves as a conventional isolated BLG. This regime is identified as a band insulator (“BI” in Fig. 3(a,b)) state and marked in red. We schematically illustrate the band alignment that lead to the band insulator state in the inset at the right upper corner of Fig. 3(a). Between these two states, a narrow region of IEI state (blue region), characterized by spontaneous layer $U(1)$ symmetry breaking, emerges along the diagonal from the upper left to the lower right. In this phase, the system exhibits a finite gap at the Fermi level due to the interlayer binding of electron-hole pair. The calculated HF band structures of IEI state is presented in Fig. 3(c), with parameters $E_{\text{CBM}} = -70$ meV and $m^*/m_0 = 0.05$, featuring a pronounced gap at chemical potential.

The restricted parameter-space window for the emergence of the IEI state can be understood as follows. The electrons on the substrate and the holes from RMG are bound together via Coulomb attraction, forming interlayer exciton with hydrogen-like orbital characteris-

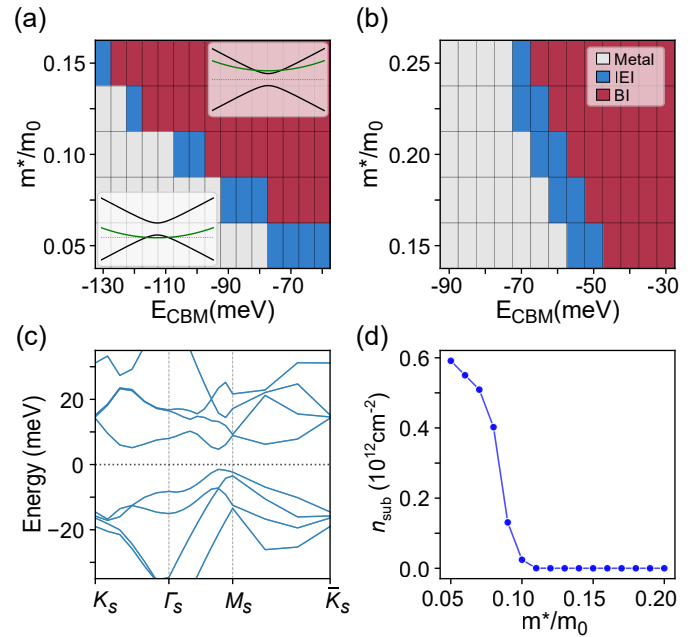


FIG. 3. (a) HF ground state phase diagram of BLG-substrate heterostructure. Insets at lower left corner and upper right corner schematically show the band structures of metallic state and band insulator state, respectively. Green lines and black lines denote substrate’s and BLG’s bands, respectively. (b) HF ground state phase diagram of TriLG-substrate heterostructure. (c) HF single particle spectrum of IEI state with $E_{\text{CBM}} = -70$ meV and effective mass $m^* = 0.05m_0$. (d) Substrate’s carrier density n_{sub} as a function of m^*/m_0 with $E_{\text{CBM}}^0 = -100$ meV.

tics. The reduced mass μ of this interlayer exciton is $1/\mu = 1/m^* + 1/2m_g^*$, where m_g^* is the effective mass of the valence band maximum of RMG and the factor of 2 comes from the valley degeneracy. The corresponding binding energy $E \propto -\mu/\epsilon_r^2$, with effective Bohr radius $\sim \epsilon_r(m_0/\mu)a_B$, where a_B is Bohr radius of hydrogen atom. Consequently, the interlayer exciton bound state is favored when the reduce mass μ is large. On the other hand, the condensation energy of IEI (in the low exciton density limit) depends on both the reduced mass and n_{sub} . However, this coupled heterostructure exhibits a distinct charge transfer mechanism: as shown in the Fig. 3(d), fixing $E_{\text{CBM}} = -100$ meV, the carrier density transferred to substrate n_{sub} , determining the maximal density of exciton, decreases with the increase of m^* due to the screening effect and Fock energy corrections. n_{sub} eventually drops to 0 for large m^* , with the disappearance of charge transfer. Therefore, with the decrease of m^* , a phase transition from the band insulator to IEI is triggered as n_{sub} increases from 0 to finite value. If the effective mass m^* is even smaller with larger n_{sub} , kinetic energy would dominate over Coulomb interaction energy, and the system becomes metallic. We note that, if the whole system is electron or hole-doped, Wigner

crystal state can be obtained at the substrate side for large m^* and/or low n_{sub} using our full-band HF approach, without imposing the Born-Oppenheimer-type treatment. This provides strong self-consistent support and corroborates the physical picture underlying the earlier Born-oppenheimer-type treatment.

In conclusion, our work establishes a comprehensive theoretical framework for RMG-insulator charge-transfer heterostructures. Starting with a self-consistent electrostatic screening model, we unveil the competition mechanism that leads to the puzzling experimental transport features, i.e., the bent and broadened charge neutrality region. We further study the correlated and topological properties of the charge-transfer heterostructures in different regimes. When the effective mass of substrate's carriers is much larger than that of RMG, the transferred carriers at the substrate may form a Wigner crystal, which imposes a superlattice electrostatic potential

to the low-energy electrons in RMG through interlayer Coulomb interactions. This suppresses the kinetic energy, and endows nontrivial topological properties to the low-energy carriers in RMG. As a result, Chern insulators emerge at integer fillings of the Wigner supercell driven by long-range electron-electron interactions. When the effective mass of substrate's carriers is comparable to that of RMG, interlayer excitonic insulator emerges at charge neutrality. Our work thus provides a unified theoretical framework that bridges charge reconstruction, topological properties and strong correlations in charge-transfer van der Waals heterostructures.

This work is supported by National Natural Science Foundation of China (grant no. 12404221 and no. U23A6002), the National Key Research and Development Program of China (grant no. 2024YFA1410400 and no. 2022YFA1604400/03) and Shanghai Science and Technology Innovation Action Plan (grant no. 24LZ1401100).

Supplemental Materials for “Correlated states in charge-transfer heterostructures based on rhombohedral multilayer graphene”

Yanran Shi, Xin Lu [†] and Jianpeng Liu [‡]

CONTENTS

Acknowledgments	5
k · p model of rhombohedral multilayer graphene	6
Fock energy correction	7
Self-consistent screening model	8
Continuum model describing rhombohedral multilayer graphene coupled to insulating substrate via interlayer Coulomb coupling	9
Renormalization of the model parameters due to interactions with remote-band electrons	12
Band-projected Hartree-Fock method	12
Full-band Hartree-Fock Method	14

k · p MODEL OF RHOMBOHEDRAL MULTILAYER GRAPHENE

The charge-transfer heterostructures based on rhombohedral multilayer graphene (RMG) described in the main text can always be divided into three parts: the RMG part, the substrate part and the interlayer Coulomb coupling between them. In this section, we present a detailed derivation of the Hamiltonian for the **k · p** model of RMG. Since we focus on the low energy physics, the non-interacting Hamiltonian of RMG can be described by a general effective continuum model directly derived from the atomistic tight-binding Hamiltonian.

We define the primitive lattice vectors of graphene unit cell as $\mathbf{a}_1 = a(1, 0)$ and $\mathbf{a}_2 = a(1/2, \sqrt{3}/2)$ with $a = 2.46 \text{ \AA}$. The corresponding reciprocal lattices are constructed as $\mathbf{b}_1 = 2\pi/a(1, -1/\sqrt{3})$ and $\mathbf{b}_2 = 2\pi/a(0, 2/\sqrt{3})$ from $\mathbf{a}_i \cdot \mathbf{b}_j = 2\pi\delta_{ij}$. The two sublattices forming honeycomb lattice are seated at $\boldsymbol{\tau}_a = a(0, -1/\sqrt{3})$ and $\boldsymbol{\tau}_b = (0, 0)$, respectively. We consider the situation that the next layer is shifted in the in-plane direction $a(0, -1/\sqrt{3})$ with respect to the previous layer, which defines the stacking chirality. The Dirac points of monolayer graphene are located at $\mathbf{K}_+ = -4\pi/3a(1, 0)$ and $\mathbf{K}_- = 4\pi/3a(1, 0)$. Then we derive the **k · p** model from the atomistic Slater-Koster tight-binding model based on carbon’s p_z -like Wannier orbitals:

$$H_{\text{RMG}}^0 = \sum_{il\alpha, jl'\alpha'} -t (\mathbf{R}_i + \boldsymbol{\tau}_\alpha + ld_0 \mathbf{e}_z - \mathbf{R}_j - \boldsymbol{\tau}_{\alpha'} - l'd_0 \mathbf{e}_z) \hat{c}_{il\alpha}^\dagger \hat{c}_{jl'\alpha'} , \quad (\text{S1})$$

where i, j represents lattice sites and $\mathbf{R}_i, \mathbf{R}_j$ represents lattice vectors in graphene. l and l' are layer indexes while α and α' are sublattice indexes. d_0 is the interlayer distance and \mathbf{e}_z is a unit vector along out-of-plane direction. $t(\mathbf{d})$

[†]lvxin@shanghaitech.edu.cn

[‡]liujp@shanghaitech.edu.cn

is hopping amplitude between two p_z orbitals displaced by vector \mathbf{d} , which is expressed in the form:

$$-t(\mathbf{d}) = V_{pp\pi} \left[1 - \left(\frac{\mathbf{d} \cdot \mathbf{e}_z}{d} \right)^2 \right] + V_{pp\sigma} \left(\frac{\mathbf{d} \cdot \mathbf{e}_z}{d} \right)^2 \quad (\text{S2})$$

$$\begin{aligned} V_{pp\pi} &= V_{pp\pi}^0 \exp \left(-\frac{|\mathbf{d}| - a/\sqrt{3}}{r_0} \right) \\ V_{pp\sigma} &= V_{pp\sigma}^0 \exp \left(-\frac{|\mathbf{d}| - d_0}{r_0} \right) \end{aligned} \quad (\text{S3})$$

where $V_{pp\pi}^0 = -2.7 \text{ eV}$, $V_{pp\sigma}^0 = 0.48 \text{ eV}$ and $r_0 = 0.184a$ [64, 65].

In our model, we consider only interlayer hopping between two nearest graphene sheets. After Fourier transformation to \mathbf{k} space, and expand the (Fourier transformed) tight-binding model in the vicinity of Dirac points, we obtain the $\mathbf{k} \cdot \mathbf{p}$ model of RMG, with the intralayer and interlayer parts of Hamiltonian expressed as

$$h_{\text{intra}}^{0,\mu} = -\hbar v_F^0 \mathbf{k} \cdot \boldsymbol{\sigma}^\mu \quad (\text{S4})$$

$$h_{\text{inter}}^{0,\mu} = \begin{pmatrix} \hbar v_\perp (\mu k_x + ik_y) & t_\perp \\ \hbar v_\perp (\mu k_x - ik_y) & \hbar v_\perp (\mu k_x + ik_y) \end{pmatrix} \quad (\text{S5})$$

$\mu = \pm$ refers to valley index. \mathbf{k} is the wave vector expanded around \mathbf{K}_+ / \mathbf{K}_- point. $\boldsymbol{\sigma}^\mu = (\mu \sigma_x, \sigma_y)$ are Pauli matrices defined in sublattice space. In term of Slater-Koster transfer integral form, $\hbar v_F^0 = 5.253 \text{ eV} \cdot \text{\AA}$ is the non-interacting band velocity of Dirac fermions in monolayer graphene. $\hbar v_\perp = 0.335 \text{ eV} \cdot \text{\AA}$ and $t_\perp = 0.34 \text{ eV} \cdot \text{\AA}$ are Slater-Koster hopping parameters. The low-energy Hamiltonian of n -layer RMG of valley μ , denoted as $H_{\text{RMG}}^{0,\mu}$, is just consisted of the intralayer term $h_{\text{intra}}^{0,\mu}$ appearing in the diagonal block (in layer space) and the interlayer term $h_{\text{inter}}^{0,\mu}$ coupling adjacent layers.

FOCK ENERGY CORRECTION

We continue to consider the Fock self-energy correction to electrons transferred from the RMG to the substrate. In the setup described in the main text, we consider the situation that the conduction band minimum (CBM) of the substrate is charge doped. These low energy electrons around the CBM are modeled as 2D electron gas, the non-interacting Hamiltonian of which is approximated by a parabolic band:

$$H_{\text{sub}}^0 = \sum_{\mathbf{k}_s} \left(\frac{\hbar^2 k_s^2}{2m^*} + E_{\text{CBM}} \right) \hat{d}^\dagger(\mathbf{k}_s) \hat{d}(\mathbf{k}_s), \quad (\text{S6})$$

where m^* is the effective mass at CBM. The operator $\hat{d}(\mathbf{k}_s)$ ($\hat{d}^\dagger(\mathbf{k}_s)$) annihilates (creates) an electron with a wave vector \mathbf{k}_s expanded around the CBM within the atomic unit cell of substrate. The E_{CBM} is the relative energy shift of CBM with respect to the CNP of RMG. For example, according to the DFT calculations, the value of E_{CBM} is -0.13 eV for CrOCl. However, long-ranged Coulomb interactions among electrons transferred to the substrate will modify the energy dispersion and consequently change the value of E_{CBM} [66, 67].

The long-ranged Coulomb interactions between electrons can be written as:

$$\hat{H}_{\text{int}} = \frac{1}{2S} \sum_{\mathbf{k}_s, \mathbf{k}'_s, \mathbf{q}_s} \sum_{\sigma, \sigma'} V(\mathbf{q}_s) \hat{d}^\dagger_{\sigma, \mathbf{k}_s + \mathbf{q}_s} \hat{d}^\dagger_{\sigma', \mathbf{k}'_s - \mathbf{q}_s} \hat{d}_{\sigma', \mathbf{k}'_s} \hat{d}_{\sigma, \mathbf{k}_s}. \quad (\text{S7})$$

In the Hartree-Fock (HF) approximation, the electron-electron interaction is decoupled at the mean-field level into the Hartree term and the Fock term:

$$\hat{H}_{\text{int}} = \frac{1}{S} \sum_{\mathbf{k}_s \sigma, \mathbf{k}'_s \sigma'} [V(0) - \delta_{\sigma \sigma'} V(\mathbf{k}'_s - \mathbf{k}_s)] n_{\mathbf{k}'_s \sigma'} \hat{d}^\dagger_{\mathbf{k}_s \sigma} \hat{d}_{\mathbf{k}_s \sigma}. \quad (\text{S8})$$

The Hartree term represents the classical electrostatic potential generated by the average charge density and the Fock term encodes the quantum-mechanical exchange effects. We subsume the Hartree term into the layer-dependent

electrostatic energy from the self-consistent screening model introduced in the next section and thus neglected here. Only the Fock term is retained, as it constitutes the primary correction of E_{CBM} . The Fock energy reads:

$$\begin{aligned}
V_{\mathbf{k}_s\sigma}^x &= -\frac{1}{S} \sum_{\mathbf{k}'_s\sigma'} \delta_{\sigma\sigma'} V(\mathbf{k}'_s - \mathbf{k}_s) n_{\mathbf{k}'_s\sigma'} \\
&= - \int \frac{d^2\mathbf{k}'_s}{4\pi^2} \frac{e^2}{2\epsilon_0\epsilon_r} \cdot \frac{1}{|\mathbf{k}'_s - \mathbf{k}_s|} n_{\mathbf{k}'_s\sigma'} \\
&= - \int_0^{k_{\text{F},\sigma}} \int_0^{2\pi} \frac{k'_s dk'_s d\theta}{4\pi^2} \frac{e^2}{2\epsilon_0\epsilon_r} \cdot \frac{1}{\sqrt{k_s^2 + k'^2_s - 2k_s k'_s \cos\theta}} \\
&= - \int_0^1 \int_0^{2\pi} dy d\theta \frac{k_{\text{F},\sigma}}{4\pi^2} \cdot \frac{e^2}{2\epsilon_0\epsilon_r} \cdot \frac{y}{\sqrt{x^2 + y^2 - 2xy \cos\theta}}.
\end{aligned} \tag{S9}$$

$V(\mathbf{k}'_s - \mathbf{k}_s) = e^2/2\epsilon_0\epsilon_r|\mathbf{k}'_s - \mathbf{k}_s|$ is the Fourier transformation of 2D long-range Coulomb potential $e^2/4\pi\epsilon_0\epsilon_r r$. S is the total area of the system. In the second line of the above derivation, we smear the sum over \mathbf{k}'_s by replacing it with an integral and then switch to cylindrical coordinates in the third line. Subsequently, we introduce the dimensionless variables x and y through the transformations $k_s = xk_{\text{F},\sigma}$ and $k'_s = yk_{\text{F},\sigma}$, where $k_{\text{F},\sigma}$ is the Fermi wave vector of spin- σ electrons. This rescaling reduces the integrand to a dimensionless form suitable for analytical evaluation.

Since we focus on the low energy electrons around the CBM of the substrate, we set $\mathbf{k}_s = 0$ ($x = 0$) and obtain the corresponding Fock energy $V_{\mathbf{k}_s=0,\sigma}^x = -\frac{e^2 k_{\text{F},\sigma}}{4\pi\epsilon_0\epsilon_r}$. Throughout this work, we consider the situation that electrons transferred to the substrate are spin degenerate. When the spin degree of freedom is taken into account, we get:

$$V_{\mathbf{k}_s=0}^x = -\frac{e^2 k_{\text{F}}}{4\pi\epsilon_0\epsilon_r} = -\frac{e^2}{4\pi\epsilon_0\epsilon_r} \sqrt{2\pi n_{\text{sub}}} \tag{S10}$$

where the Fermi wave vector of substrate's low energy electrons is defined by $k_{\text{F}} = \sqrt{2\pi n_{\text{sub}}}$. It is exactly the expression of Fock energy correction $\delta E_{\text{CBM}} = -\frac{e^2}{4\pi\epsilon_0\epsilon_r} \sqrt{2\pi n_{\text{sub}}}$ mentioned in the main text.

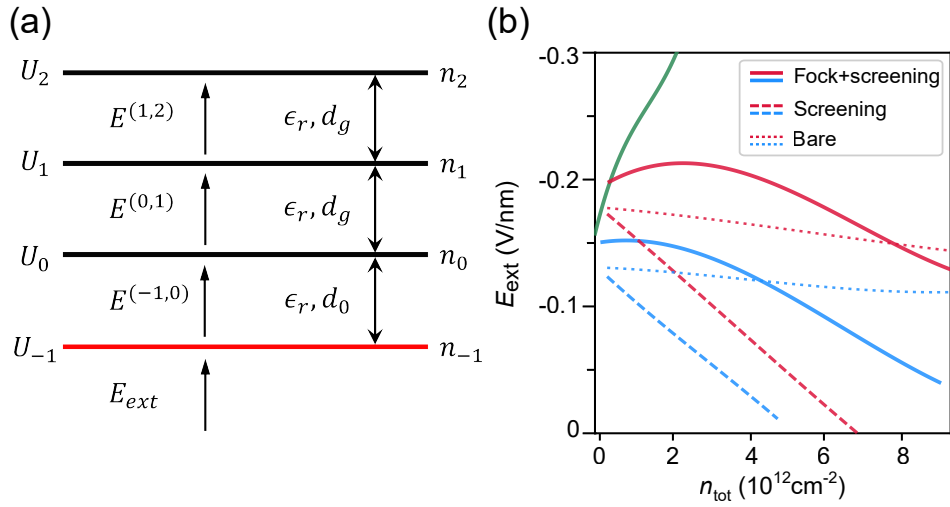
SELF-CONSISTENT SCREENING MODEL

It has been well known that an externally applied out-of-plane electric field experiences significant screening thanks to the redistribution of electrons across different layers in multilayer graphene system [68–73]. In this section, we develop a self-consistent screening model for charge transfer heterostructures based on RMG that integrates the self-consistent Hartree screening method described in Ref. [73] to account for the conventional screening effect along with the Fock energy correction to E_{CBM} discussed in the above section. This framework enables the determination of the layer-resolved charge density distribution and relative electrostatic energy of graphene layers with respect to the surface of the substrate.

Under an out-of-plane electric field E_{ext} , each graphene layer gets a relative electrostatic energy shift with respect to the substrate, which is expressed as $U_d = eE_{\text{ext}}(d_0 + ld_g)$ and added into the diagonal part in the Hamiltonian of RMG. The $l = 0, 1, 2, \dots$ is layer index of RMG. d_0 is the distance between the surface of substrate and the bottom graphene layer. $d_g = 3.35 \text{ \AA}$ is the intrinsic interlayer distance of the RMG. Solving the total Hamiltonian $H^0 = H_{\text{RMG}}^0 + H_{\text{sub}}^0$ that consists of the $\mathbf{k} \cdot \mathbf{p}$ model of RMG and the non-interacting Hamiltonian of electron transferred to the substrate, we retrieve the layer-resolved excess electron density distribution. This quantum-mechanically computed layer-resolved excess electron density then serves as the source term in the classical Poisson equation, which is solved with a dielectric constant ϵ_r to update the screened electrostatic potential. Simultaneously, the Fock energy correction δE_{CBM} , evaluated from the carrier density in substrate n_{sub} , is added to the on-site energy of substrate. By performing a self-consistent solution of the aforementioned screening process, the actual layer-resolved charge distribution and the corresponding relative electrostatic potential energy shift of graphene layers with respect to the surface of substrate at equilibrium can be obtained.

From Gauss' law, taking the trilayer graphene-substrate heterostructure as an example, the electric field $E^{(l,l+1)}$ between the l -th and $(l+1)$ -th layers is

$$\begin{aligned}
E^{(l,l+1)} - E_{\text{ext}} &= -\frac{n_l e}{\epsilon_0\epsilon_r} \quad \text{if } l = -1, \\
E^{(l,l+1)} - E^{(l-1,l)} &= -\frac{n_l e}{\epsilon_0\epsilon_r} \quad \text{if } l \geq 0,
\end{aligned} \tag{S11}$$



Supplementary Figure 1. (a) Schematic illustration of the self-consistent screening model of vertical electric field applied to trilayer graphene-based charge transfer heterostructure. ϵ_r is the dielectric constant. d_0 denotes the interlayer distance between the surface of substrate and the bottom graphene layer of RMG while d_g denotes the intrinsic interlayer distance of the RMG. (b) Calculated phase boundaries for BLG-CrOCl under three levels of theoretical treatment: with initial band alignment denoted by “Bare” (dotted lines), with dielectric screening included denoted by “Screening” (dashed lines), and with both screening and Fock energy correction incorporated denoted by “Screening+Fock” (solid lines). The green, blue, and red curves denote, respectively, the phase boundaries separating (i) non-charge-transfer and charge-transferred regions, (ii) the hole-doped and CNP regions, and (iii) the CNP and electron-doped regions.

for $l = -1, 0, 1, 2$. The negative value of l corresponds to the surface of the substrate while nonnegative l correspond to RMG. ϵ_r is the dielectric constant of RMG-substrate heterostructure and n_l is defined with respect to intralayer charge neutral point, i.e., positive if there is excess electron and vice versa. Then the layer-resolved on-site energies U_l are set given that

$$\begin{aligned} U_l &= U_{l-1} + eE^{(l-1,l)}d_0 & \text{if } l = 0, \\ U_l &= U_{l-1} + eE^{(l-1,l)}d_g & \text{if } l \geq 1. \end{aligned} \quad (\text{S12})$$

Where we take the substrate surface as the reference point with zero electrostatic potential.

In our calculations, the \mathbf{k} mesh is 600×600 . To elucidate the enhancement of the dielectric screening effect with increasing layer number, we use the dielectric constant $\epsilon_r = 8, 16$ for the BLG-CrOCl and TriLG-CrOCl, respectively.

We have proposed that the characteristic features of RMG charge-transfer heterostructure, the pronounced “broad” and “bent” CNP region of RMG, are attributed to the competition between the conventional screening effect and the Fock energy correction in the main text. To facilitate interpretation of this analysis, Supplementary Figure 1(b) illustrates the evolution of the upper (red) and lower (blue) boundary of the CNP region across three levels of theoretical consideration. The nearly horizontal dotted lines (labeled “Bare”) denote the boundaries of CNP region obtained considering neither dielectric screening nor Fock energy correction. Inclusion of dielectric screening yields steeper linear dashed boundaries (labeled “Screening”). Further incorporation of the Fock energy correction results in curved solid lines (labeled “Screening+Fock”), which delineate the bent CNP boundaries and enclose a markedly expanded CNP region. Hence, our approach captures the essential physics governing interlayer charge redistribution and dielectric screening, thereby establishing a reliable foundation for understanding electron-electron interaction effects in graphene-based charge-transfer heterostructures.

CONTINUUM MODEL DESCRIBING RHOMBOHEDRAL MULTILAYER GRAPHENE COUPLED TO INSULATING SUBSTRATE VIA INTERLAYER COULOMB COUPLING

Now we discuss the interlayer coupling between electrons within RMG and electrons transferred to substrate. Since the interlayer hopping amplitude decays exponentially with interlayer separation d_0 while the interlayer Coulomb

interaction decays only as a power law, the former can be safely neglected when the interlayer separation d_0 and the lattice mismatch is large. Hence, the low energy electrons in this system have an emergent approximate layer U(1) symmetry. The interlayer coupling is dominated by the long-range Coulomb potential between electrons in the substrate and those in the RMG. In this regime, we can treat such Coulomb-coupled two-component systems in the “Born-Oppenheimer” type approximation, where the wavefunction of the ground state can be written as the product of that of RMG and that of substrate, i.e.,

$$|\Psi\rangle = |\Psi\rangle_c \otimes |\Psi\rangle_d, \quad (\text{S13})$$

where the ground wavefunction with low index c and d represents that of RMG and substrate, respectively. As discussed in the main text, given that the carrier density of the substrate n_{sub} is below a threshold and the effective mass m^* at CBM is large, long-wavelength charge order state can be induced at the surface of the substrate via Coulomb interactions, with electrons localized into a superlattice. The geometry of superlattice is determined by the long-wavelength order at the interface. In our calculation, we set the superlattice to be triangular. The Hamiltonian between RMG and the insulating substrate reads:

$$\hat{H}_{\text{G-S}} = \int d^2\mathbf{r} d^2\mathbf{r}' \sum_{\sigma\sigma'} \hat{\psi}_{c,\sigma}^\dagger(\mathbf{r}) \hat{\psi}_{d,\sigma'}^\dagger(\mathbf{r}') V |\mathbf{r} - \mathbf{r}'| \hat{\psi}_{d,\sigma'}(\mathbf{r}') \hat{\psi}_{c,\sigma}(\mathbf{r}), \quad (\text{S14})$$

where the field operators $\hat{\psi}(\mathbf{r})$ with subscript c and d act on electrons in RMG and substrate, respectively. $V(\mathbf{r} - \mathbf{r}') = e^2/(4\pi\epsilon_0\epsilon_r|\mathbf{r} - \mathbf{r}'|)$ represents the three-dimensional Coulomb potential, with ϵ_0 and ϵ_r denoting the vacuum permittivity and the relative dielectric constant of the environment, respectively. l is the layer index. σ is spin index.

In terms of Wannier functions $\phi_{l\alpha}$ localized on the atomic lattice sites \mathbf{a}_i of l th graphene layer within RMG and $\tilde{\phi}$ localized on superlattice sites \mathbf{R}_i formed on the surface of substrate, the field operators can be represented as:

$$\begin{aligned} \hat{\psi}_{c,\sigma}^\dagger(\mathbf{r}) &= \sum_{i,l\alpha} \phi_{l\alpha}^*(\mathbf{r} - \mathbf{a}_i - \boldsymbol{\tau}_\alpha - d_l \hat{\mathbf{z}}) \chi_\sigma^\dagger \hat{c}_{il\alpha,\sigma}^\dagger \\ \hat{\psi}_{d,\sigma}^\dagger(\mathbf{r}) &= \sum_i \tilde{\phi}^*(\mathbf{r} - \mathbf{R}_i) \chi_\sigma^\dagger \hat{d}_{i,\sigma}^\dagger \end{aligned} \quad (\text{S15})$$

Here i, l, α, σ represent lattice site index, layer index, sublattice index and spin index, respectively. χ_σ is two component spinor wavefunction. It is worthwhile to note that here the Bravais lattice sites and the corresponding Wannier functions for the substrate refer to those of the spontaneously generated charge ordered superlattice, not the atomic lattices of the substrate. After transforming the Hamiltonian $\hat{H}_{\text{G-S}}$ into the Wannier basis, we obtain:

$$\hat{H}_{\text{G-S}} = \sum_{\substack{\sigma,\sigma' \\ \alpha,\alpha' \\ l,l'}} \sum_{\substack{i,i' \\ j,j'}} U_{il\alpha j,i' l' \alpha' j'}^{\sigma,\sigma'} \hat{c}_{il\alpha,\sigma}^\dagger \hat{d}_{i',\sigma'}^\dagger \hat{d}_{j',\sigma'} \hat{c}_{i' l' \alpha',\sigma}^\dagger \quad (\text{S16})$$

with

$$U_{il\alpha j,i' l' \alpha' j'}^{\sigma,\sigma'} = \int d^2\mathbf{r} d^2\mathbf{r}' \phi_{l\alpha}^*(\mathbf{r} - \mathbf{a}_i - \boldsymbol{\tau}_\alpha - d_l \hat{\mathbf{z}}) \tilde{\phi}^*(\mathbf{r} - \mathbf{R}_j) \tilde{\phi}(\mathbf{r} - \mathbf{R}_{j'}) \phi_{l' \alpha'}^*(\mathbf{r} - \mathbf{a}_{i'} - \boldsymbol{\tau}_{\alpha'} - d_{l'} \hat{\mathbf{z}}) \chi_\sigma^\dagger \chi_{\sigma'}^\dagger \chi_{\alpha'} \chi_\alpha. \quad (\text{S17})$$

We assume that the Wannier functions are so localized that

$$\phi_{l\alpha}^*(\mathbf{r} - \mathbf{a}_i - \boldsymbol{\tau}_\alpha - d_l \hat{\mathbf{z}}) \phi_{l' \alpha'}^*(\mathbf{r} - \mathbf{a}_{i'} - \boldsymbol{\tau}_{\alpha'} - d_{l'} \hat{\mathbf{z}}) \approx 0 \quad \text{if } (i, l, \alpha) \neq (i', l', \alpha') \quad (\text{S18})$$

$$\tilde{\phi}^*(\mathbf{r} - \mathbf{R}_j) \tilde{\phi}(\mathbf{r} - \mathbf{R}_{j'}) \approx 0 \quad \text{if } j \neq j' \quad (\text{S19})$$

$$|\phi_{l\alpha}(\mathbf{r} - \mathbf{a}_i - \boldsymbol{\tau}_\alpha - d_l \hat{\mathbf{z}})|^2 \approx \delta^2(\mathbf{r} - \mathbf{a}_i - \boldsymbol{\tau}_\alpha - d_l \hat{\mathbf{z}}) \quad (\text{S20})$$

$$|\tilde{\phi}(\mathbf{r} - \mathbf{R}_j)|^2 \approx \delta^2(\mathbf{r} - \mathbf{R}_j), \quad (\text{S21})$$

where $\delta^2(\mathbf{r})$ is 2D Dirac δ -function distribution. Then, the expression of $U_{il\alpha j,i' l' \alpha' j'}^{\sigma,\sigma'}$ can be simplified to $U_{il\alpha j} \delta_{i,i'} \delta_{l,l'} \delta_{\alpha,\alpha'} \delta_{j,j'}$ with the Kronecker delta $\delta_{\mu,\nu}$ and $U_{il\alpha,j} = V(|\mathbf{a}_i + \boldsymbol{\tau}_\alpha + d_l \hat{\mathbf{z}} - \mathbf{R}_j|)$.

Next, using the Fourier transformation

$$\begin{aligned} \hat{c}_{il\alpha,\sigma} &= \frac{1}{N_c} \sum_{\mathbf{k}} e^{i\mathbf{k}\cdot\mathbf{a}_i} \hat{c}_{l\alpha,\sigma}(\mathbf{k}) \\ \hat{d}_{i,\sigma} &= \frac{1}{N_d} \sum_{\tilde{\mathbf{k}}} e^{i\tilde{\mathbf{k}}\cdot\mathbf{R}_i} \hat{d}_{\sigma}(\tilde{\mathbf{k}}) \end{aligned} \quad (\text{S22})$$

where N_c and N_d are the number of lattice sites for electron in RMG and the substrate, respectively. \mathbf{k} and $\tilde{\mathbf{k}}$ are the wavevectors in the Brillouin zone of graphene and that of the long-wavelength superlattice in the substrate, respectively. Then we can write the Hamiltonian $\hat{H}_{\text{G-S}}$ in reciprocal space:

$$\hat{H}_{\text{G-S}} = \frac{1}{N_c N_d} \sum_{\mathbf{k}, \mathbf{k}'} \sum_{\sigma, \sigma'} U_{il\alpha j} e^{i(\mathbf{k}' - \mathbf{k}) \cdot (\mathbf{a}_i - \mathbf{R}_j)} e^{i(\mathbf{k}' - \mathbf{k} + \tilde{\mathbf{k}}' - \tilde{\mathbf{k}}) \cdot \mathbf{R}_j} \hat{c}_{l\alpha, \sigma}^\dagger(\mathbf{k}) \hat{d}_{\sigma'}^\dagger(\tilde{\mathbf{k}}) \hat{d}_{\sigma'}(\tilde{\mathbf{k}}') \hat{c}_{l'\alpha', \sigma}(\mathbf{k}'). \quad (\text{S23})$$

We define $\tilde{\mathbf{R}} = \mathbf{a}_i - \mathbf{R}_j$ and set $\mathbf{k} - \mathbf{k}' = \mathbf{q} = \tilde{\mathbf{q}} + \mathbf{G}$, where $\tilde{\mathbf{q}}$ is wave vector defined within the mini-Brillouin zone of the superlattice and \mathbf{G} is a reciprocal vector of the superlattice. Utilizing the identity $\sum_j e^{i(\tilde{\mathbf{k}}' - \tilde{\mathbf{k}} - \tilde{\mathbf{q}} - \mathbf{G}) \cdot \tilde{\mathbf{R}}_j} = N_d \delta_{\tilde{\mathbf{k}}' - \tilde{\mathbf{k}}, \tilde{\mathbf{q}}}$, the above expression is simplified as:

$$\hat{H}_{\text{G-S}} = \sum_{\sigma\sigma', l\alpha} \sum_{\substack{\mathbf{k}, \tilde{\mathbf{k}} \\ \tilde{\mathbf{q}}, \mathbf{G}}} \tilde{V}(\tilde{\mathbf{q}} + \mathbf{G}) \hat{c}_{\sigma, l\alpha}^\dagger(\mathbf{k}) \hat{d}_{\sigma'}^\dagger(\tilde{\mathbf{k}}) \hat{d}_{\sigma'}(\tilde{\mathbf{k}} + \tilde{\mathbf{q}}) \hat{c}_{\sigma, l\alpha}(\mathbf{k} - \tilde{\mathbf{q}} - \mathbf{G}). \quad (\text{S24})$$

The expression of interlayer coupling $\tilde{V}(\tilde{\mathbf{q}} + \mathbf{G})$ is:

$$\begin{aligned} \tilde{V}(\tilde{\mathbf{q}} + \mathbf{G}) &= \frac{1}{N_c} \sum_i V(|\mathbf{a}_i + \boldsymbol{\tau}_\alpha + d_l \hat{\mathbf{z}} - \mathbf{R}_j|) e^{-i(\tilde{\mathbf{q}} + \mathbf{G}) \cdot (\mathbf{a}_i - \mathbf{R}_j)} \\ &= \frac{1}{N_c} \sum_{\tilde{\mathbf{R}}} V(|\boldsymbol{\tau}_\alpha + d_l \hat{\mathbf{z}} + \tilde{\mathbf{R}}|) e^{-i(\tilde{\mathbf{q}} + \mathbf{G}) \cdot \tilde{\mathbf{R}}} \\ &= \frac{1}{N_d \Omega_d} \int d^2 \mathbf{r} V(|\mathbf{r} + \boldsymbol{\tau}_\alpha + d_l \hat{\mathbf{z}}|) e^{-i(\tilde{\mathbf{q}} + \mathbf{G}) \cdot \mathbf{r}} \\ &= \frac{e^2}{2\epsilon_0 \epsilon_r N_d \Omega_d} \frac{e^{-|\tilde{\mathbf{q}} + \mathbf{G}| d_l}}{|\tilde{\mathbf{q}} + \mathbf{G}|} \end{aligned} \quad (\text{S25})$$

where Ω_d is the area of the superlattice unit cell. In the third line of the above derivation, we smear the sum over $\tilde{\mathbf{R}}$ by replacing it with an integral over the surface $S = N_d \Omega_d = N_c \Omega_c$ with Ω_c representing the area of graphene's unit-cell since we are interested in the physics in the length scale of the superlattice \mathbf{R}_j , which is supposed to much larger than that of graphene. Finally, the last line is the 2D partial Fourier transformation of the 3D Coulomb potential.

Since we concentrate on low energy physics, the operators of the electrons within RMG are introduced a valley index μ . We neglected the intervalley interactions because of the exponential decay of $\tilde{V}(\tilde{\mathbf{q}} + \mathbf{G})$ and rewrite the Hamiltonian $\hat{H}_{\text{G-S}}$ as.

$$\hat{H}_{\text{G-S}} = \sum_{\mu l\alpha} \sum_{\substack{\mathbf{k}, \tilde{\mathbf{k}} \\ \tilde{\mathbf{q}}, \mathbf{G}}} \tilde{V}(\tilde{\mathbf{q}} + \mathbf{G}) \hat{c}_{\sigma l\mu\alpha}^\dagger(\mathbf{k}) \hat{d}_{\sigma'}^\dagger(\tilde{\mathbf{k}}) \hat{d}_{\sigma'}(\tilde{\mathbf{k}} + \tilde{\mathbf{q}}) \hat{c}_{\sigma l\mu\alpha}(\mathbf{k} - \tilde{\mathbf{q}} - \mathbf{G}). \quad (\text{S26})$$

In the Hartree approximation by contracting fermion operators with subscript c and d separately, we obtain:

$$\begin{aligned} \hat{H}_{\text{G-S}} &= \sum_{\sigma\mu, l\alpha} \sum_{\mathbf{k}, \mathbf{G}} V(\mathbf{G}) \sum_{\sigma', \tilde{\mathbf{k}}'} \left\langle \hat{d}_{\sigma'}^\dagger(\tilde{\mathbf{k}}) \hat{d}_{\sigma'}(\tilde{\mathbf{k}}) \right\rangle \hat{c}_{\sigma\mu l\alpha}^\dagger(\mathbf{k}) \hat{c}_{\sigma\mu l\alpha}(\mathbf{k} - \mathbf{G}) \\ &= \nu_s N_d \sum_{\sigma\mu, l\alpha} \sum_{\mathbf{k}, \mathbf{G}} \tilde{V}(\mathbf{G}) \hat{c}_{\sigma\mu l\alpha}^\dagger(\mathbf{k}) \hat{c}_{\sigma\mu l\alpha}(\mathbf{k} - \mathbf{G}) \end{aligned} \quad (\text{S27})$$

where ν_s denotes the number of electrons within a superlattice unit cell. Writing $\mathbf{k} = \tilde{\mathbf{k}} + \mathbf{G}$ with \mathbf{G} in the superlattice reciprocal lattice, the form of the coupling between RMG and insulating substrate reads:

$$\hat{H}_{\text{G-S}} = \sum_{\sigma\mu l\alpha} \sum_{\mathbf{G}, \mathbf{Q}} \tilde{U}_s(\mathbf{Q}) \hat{c}_{\sigma\mu l\alpha, \mathbf{G} + \mathbf{Q}}^\dagger(\tilde{\mathbf{k}}) \hat{c}_{\sigma\mu l\alpha, \mathbf{G}}(\tilde{\mathbf{k}}), \quad (\text{S28})$$

where $\tilde{U}_s(\mathbf{Q}) = \frac{\nu_s e^2}{2\epsilon_0 \epsilon_r \Omega_d} \frac{e^{-|\mathbf{Q}| d}}{|\mathbf{Q}|}$.

Incorporating the superlattice potential, we obtain the low-energy effective continuum model for the RMG part:

$$\hat{H}_{\text{RMG}}^{0,\mu} = \hat{H}_{\text{RMG}}^{0,\mu} + U_s(\mathbf{r}) + U_d \quad (\text{S29})$$

where U_d is the electrostatic on-site energy obtained from self-consistent screening model. $U_s(\mathbf{r})$ is the background superlattice potential with the period $U_s(\mathbf{r}) = U_s(\mathbf{r} + \mathbf{L}_s)$, whose Fourier components are exactly $\tilde{U}_s(\mathbf{Q})$. Such a continuum-model description is adopted throughout the calculations within “Born-Oppenheimer-type” treatment. Given that $L_s \geq a$ ($a = 2.46 \text{ \AA}$ is the lattice constant of graphene) is always fulfilled with low carrier density of the substrate n_{sub} .

RENORMALIZATION OF THE MODEL PARAMETERS DUE TO INTERACTIONS WITH REMOTE-BAND ELECTRONS

In our work, we mostly focus on the low-energy physics around charge neutrality point. We set up a low-energy window marked by E_C^* which roughly includes three conduction subbands and three valence subbands per spin per valley. Electron-electron interactions become important and non-perturbative within this low-energy window within E_C^* , while they can be approximately treated as perturbations to single-particle energy outside E_C^* . We call the electrons within the low-energy window as low-energy electrons, while those out-side E_C^* as remote-band electrons. Although we focus on the low-energy physics, the occupied remote-band electrons indeed play an important role considering e - e interactions. The electrons in the filled remote bands will act through long-ranged Coulomb potential upon the properties of low-energy electrons. As a result, an effective low-energy single-particle Hamiltonian (within E_C^*) would have parameters in general larger in amplitudes than the non-interacting ones. For example, it is well known that the Fermi velocity around the Dirac point in graphene would be amplified by the filled Dirac Fermi sea [74]. We take into account this effect using perturbative renormalization group (RG) approach [73, 75]. Without going into detailed derivations, we directly write down the expressions of the renormalized model parameters as already reported in Ref. [73]

$$v_F(E_C^*) = v_F^0 \left(1 + \frac{\alpha_0}{4\epsilon_r} \log \frac{E_C}{E_C^*} \right) \quad (\text{S30a})$$

$$t_{\perp}(E_C^*) = t_{\perp} \left(1 + \frac{\alpha_0}{4\epsilon_r} \log \frac{E_C}{E_C^*} \right) \quad (\text{S30b})$$

$$v_{\perp}(E_C^*) = v_{\perp} . \quad (\text{S30c})$$

Here E_C is the largest energy cutoff of the continuum model above which the Dirac-fermion description to graphene would no longer be valid. $\alpha_0 = e^2/4\pi\epsilon_0\hbar v_F$ is the effective fine structure constant of graphene. We refer the readers to Ref.[20, 73] for detailed derivations of the above equations.

Using the aforementioned low-energy effective continuum model for RMG with parameters corrected by RG approach, we have calculated the single-particle properties for bilayer (BLG) and trilayer (TriLG) graphene on a CrOCl substrate. In the main text, isolated flat bands emergent in the energy band structure of BLG with parameters $E_{\text{ext}} = -0.225 \text{ V/nm}$ and $n_{\text{tot}} = 8.34 \times 10^{11} \text{ cm}^{-2}$ in the presence of superlattice potential U_s , as illustrated in Fig. 1(b) of the main text. Furthermore, in Supplementary Figure 2, we present the Chern number phase diagrams of the lowest conduction band (LCB) for bilayer graphene (BLG) (a) and trilayer graphene (TriLG) (b), both of which display a nonzero Chern number $|C| = 1$ across nearly the entire charge-transfer region. These nontrivial topological flat bands amplify interactions effect and potentially promote the formation of topological correlated states.

BAND-PROJECTED HARTREE-FOCK METHOD

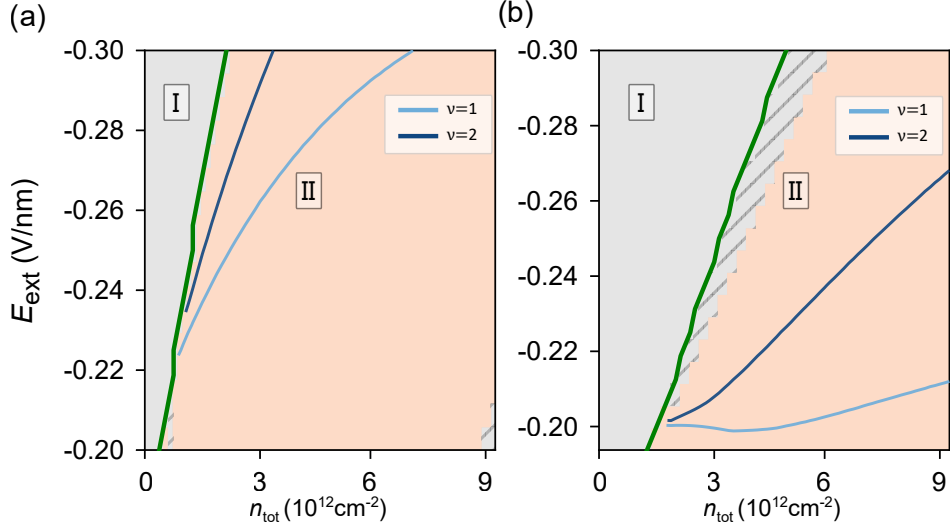
In this section, we provide the derivation of the e - e interaction Hamiltonian in the Hartree-Fock (HF) approximation projected to the band basis.

We consider the e - e Coulomb interactions

$$\hat{V}_{\text{ee}} = \frac{1}{2} \int d^2r d^2r' \sum_{\sigma, \sigma'} \hat{\psi}_{\sigma}^{\dagger}(\mathbf{r}) \hat{\psi}_{\sigma'}^{\dagger}(\mathbf{r}') V_c(|\mathbf{r} - \mathbf{r}'|) \hat{\psi}_{\sigma'}(\mathbf{r}') \hat{\psi}_{\sigma}(\mathbf{r}) \quad (\text{S31})$$

where $\hat{\psi}_{\sigma}(\mathbf{r})$ is real-space electron annihilation operator at \mathbf{r} with spin σ . Such interaction can be expressed in Wannier basis as

$$\hat{V}_{\text{ee}} = \frac{1}{2} \sum_{ii'jj'} \sum_{l_1l_1'l_2l_2'} \sum_{\alpha\alpha'\beta\beta'} \sum_{\sigma\sigma'} \hat{c}_{i,\sigma l_1\alpha}^{\dagger} \hat{c}_{i',\sigma' l_1'\alpha'}^{\dagger} V_{ij,ij'}^{\alpha\beta l_1l_2\sigma, \alpha'\beta' l_1'l_2'\sigma'} \hat{c}_{j',\sigma' l_2'\beta'} \hat{c}_{j,\sigma l_2\beta} , \quad (\text{S32})$$



Supplementary Figure 2. Phase diagrams of the Chern number for the LCB of BLG-CrOCl (a) and TriLG-CrOCl (b), computed using the effective continuum model of RMG with parameters renormalized via the RG approach. The green solid line represent the phase boundary between no charge transfer region and charge transfer region. The non-zero Chern number $|C| = 1$ region is marked by light orange. The shaded regions correspond to parameters where the lowest conduction band (LCB) has a direct gap separating it with high-energy bands $\lesssim 1$ meV, precluding a well-defined Chern number in numerical evaluation due to finite mesh. Along iso-filling lines with filling factors $\nu = 1$ and $\nu = 2$, however, the LCB is well isolated, enabling unambiguous evaluation of its topological invariant.

where

$$\begin{aligned}
 & V_{ij,i'j'}^{\alpha\beta l_1 l_2 \sigma, \alpha' \beta' l'_1 l'_2 \sigma'} \\
 &= \int d^2r d^2r' V_c(|\mathbf{r} - \mathbf{r}'|) \phi_{l_1, \alpha}^*(\mathbf{r} - \mathbf{R}_i - \boldsymbol{\tau}_{l_1, \alpha}) \phi_{l_2, \beta}(\mathbf{r} - \mathbf{R}_j - \boldsymbol{\tau}_{l_2, \beta}) \phi_{l'_1, \alpha'}^*(\mathbf{r} - \mathbf{R}'_i - \boldsymbol{\tau}_{l'_1, \alpha'}) \phi_{l'_2, \beta'}(\mathbf{r} - \mathbf{R}'_j - \boldsymbol{\tau}_{l'_2, \beta'}) \\
 & \quad \times \chi_\sigma^\dagger \chi_{\sigma'}^\dagger \chi_{\sigma'} \chi_\sigma.
 \end{aligned} \tag{S33}$$

Here i , α , l_1 (l_2), and σ refer to atomic lattice vectors, sublattice index, layer index and spin index, respectively. ϕ is Wannier function and χ is the two-component spinor wave function. We further assume that the “density-density” like interaction is dominant in the system, i.e., $V_{ij,i'j'}^{\alpha\beta l_1 l_2 \sigma, \alpha' \beta' l'_1 l'_2 \sigma'} \approx V_{ii,i'i'}^{\alpha\alpha l_1 l_1 \sigma, \alpha' \alpha' l'_1 l'_1 \sigma'} \equiv V_{i\sigma l\alpha, i'\sigma' l'\alpha'}$, then the Coulomb interaction is simplified

$$\begin{aligned}
 \hat{V}_{ee} &= \frac{1}{2} \sum_{ii'} \sum_{\alpha\alpha', ll'} \sum_{\sigma\sigma'} \hat{c}_{i, \sigma l\alpha}^\dagger \hat{c}_{i', \sigma' l'\alpha}^\dagger V_{i\sigma l\alpha, i'\sigma' l'\alpha'} \hat{c}_{i', \sigma' l'\alpha'} \hat{c}_{i, \sigma l\alpha} \\
 & \approx \frac{1}{2} \sum_{il\alpha \neq i'l'\alpha'} \sum_{\sigma\sigma'} \hat{c}_{i, \sigma l\alpha}^\dagger \hat{c}_{i', \sigma' l'\alpha'}^\dagger V_{il\alpha, i'l'\alpha'} \hat{c}_{i', \sigma' l'\alpha'} \hat{c}_{i, \sigma l\alpha}
 \end{aligned}$$

Here we neglect atomistic on-site Coulomb interactions which is at least one order of magnitude weaker than long-range inter-site Coulomb interactions in the context of moiré superlattice and other long-period superlattices [76]. Given that the electron density is low (10^{12} cm $^{-2}$ in our problem), the chance that two electrons meet at the same atomic site is very low. Therefore, the Coulomb interactions between two electrons are mostly contributed by the inter-site ones.

In order to model the screening effects and capture the layer dependence of Coulomb interactions in multilayer graphene, we introduce the following Coulomb potential in momentum space

$$\begin{aligned}
 V_{ll}(\mathbf{q}) &= \frac{e^2}{2\Omega_d \epsilon_r \epsilon_0 \sqrt{q^2 + \kappa^2}} \\
 V_{ll'}(\mathbf{q}) &= \frac{e^2}{2\Omega_d \epsilon_r \epsilon_0 q} e^{-q|l-l'|d_0}, \quad \text{if } l \neq l'
 \end{aligned} \tag{S34}$$

where Ω_d is the area of the superlattice's primitive cell and $\kappa = 1/400 \text{ \AA}^{-1}$ is the inverse screening length.

Since we are interested in the low-energy bands, the intersite Coulomb interactions can be divided into the intra-valley term and the inter-valley term. The intervalley term is at least two orders of magnitudes weaker than the intravalley one in our system because of the small Brillouin zone of the superlattice, thus is neglected in our present study. The intra-valley term \hat{V}^{intra} is expressed as

$$\hat{V}^{\text{intra}} = \frac{1}{2N_s} \sum_{\alpha\alpha', ll'} \sum_{\mu\mu', \sigma\sigma'} \sum_{\mathbf{k}\mathbf{k}'\mathbf{q}} V_{ll'}(\mathbf{q}) \hat{c}_{\sigma\mu l\alpha}^\dagger(\mathbf{k} + \mathbf{q}) \hat{c}_{\sigma'\mu' l'\alpha'}^\dagger(\mathbf{k}' - \mathbf{q}) \hat{c}_{\sigma'\mu' l'\alpha'}(\mathbf{k}') \hat{c}_{\sigma\mu l\alpha}(\mathbf{k}) , \quad (\text{S35})$$

where N_s is the total number of the superlattice's sites.

The electron annihilation operator can be transformed from the original basis to the band basis:

$$\hat{c}_{\sigma\mu l\alpha}(\mathbf{k}) \equiv \hat{c}_{\sigma\mu l\alpha}\mathbf{G}(\tilde{\mathbf{k}}) = \sum_n C_{\mu l\alpha\mathbf{G}, n}(\tilde{\mathbf{k}}) \hat{c}_{\sigma\mu, n}(\tilde{\mathbf{k}}) , \quad (\text{S36})$$

where $C_{\mu l\alpha\mathbf{G}, n}(\tilde{\mathbf{k}})$ is the expansion coefficient in the n -th Bloch eigenstate at $\tilde{\mathbf{k}}$ of valley μ :

$$|\sigma\mu, n; \tilde{\mathbf{k}}\rangle = \sum_{l\alpha\mathbf{G}} C_{\mu l\alpha\mathbf{G}, n}(\tilde{\mathbf{k}}) |\sigma, \mu, l, \alpha, \mathbf{G}; \tilde{\mathbf{k}}\rangle . \quad (\text{S37})$$

We note that the non-interacting Bloch functions are spin degenerate. Using the transformation given in Eq. (S36), the intra-valley Coulomb interaction can be written in the band basis

$$\begin{aligned} \hat{V}^{\text{intra}} = & \frac{1}{2N_s} \sum_{\tilde{\mathbf{k}}\tilde{\mathbf{k}}'\tilde{\mathbf{q}}} \sum_{\mu\mu'} \sum_{\substack{nm \\ n'm'}} \left(\sum_{\mathbf{Q}} V_{ll'}(\mathbf{Q} + \tilde{\mathbf{q}}) \Omega_{nm, n'm'}^{\mu l, \mu' l'}(\tilde{\mathbf{k}}, \tilde{\mathbf{k}}', \tilde{\mathbf{q}}, \mathbf{Q}) \right) \\ & \times \hat{c}_{\sigma\mu, n}^\dagger(\tilde{\mathbf{k}} + \tilde{\mathbf{q}}) \hat{c}_{\sigma'\mu', n'}^\dagger(\tilde{\mathbf{k}}' - \tilde{\mathbf{q}}) \hat{c}_{\sigma'\mu', m'}(\tilde{\mathbf{k}}') \hat{c}_{\sigma\mu, m}(\tilde{\mathbf{k}}) \end{aligned} \quad (\text{S38})$$

where the form factor $\Omega_{nm, n'm'}^{\mu l, \mu' l'}$ are written respectively as

$$\Omega_{nm, n'm'}^{\mu l, \mu' l'}(\tilde{\mathbf{k}}, \tilde{\mathbf{k}}', \tilde{\mathbf{q}}, \mathbf{Q}) = \sum_{\alpha\alpha' \mathbf{G}\mathbf{G}'} C_{\mu l\alpha\mathbf{G}+\mathbf{Q}, n}^*(\tilde{\mathbf{k}} + \tilde{\mathbf{q}}) C_{\mu' l'\alpha'\mathbf{G}'-\mathbf{Q}, n'}^*(\tilde{\mathbf{k}}' - \tilde{\mathbf{q}}) C_{\mu' l'\alpha'\mathbf{G}', m'}(\tilde{\mathbf{k}}') C_{\mu l\alpha\mathbf{G}, m}(\tilde{\mathbf{k}}) . \quad (\text{S39})$$

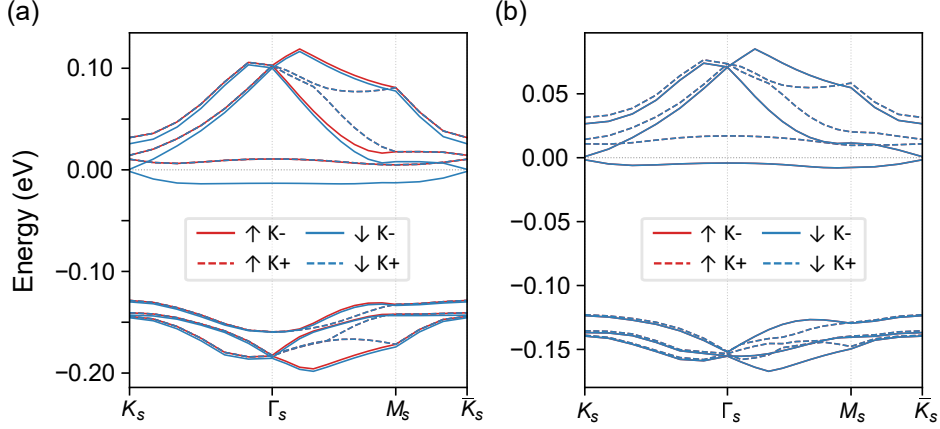
In our calculations, the long-range Coulomb interactions are projected onto the wavefunctions of three conduction bands and three valence bands (per valley per spin) obtained from the RG-corrected low-energy continuum model. Then we carry out unrestricted HF calculations within this 24-band low-energy subspace (including spin and valley degrees of freedom). To explore possible symmetry-broken phases, we consider 32 distinct trial initial states, each characterized by order parameters of the form $s^{0,z}\tau^a\sigma^b$ with $a, b = 0, x, y, z$, where s , τ and σ denote Pauli matrices acting in spin, valley, and sublattice spaces, respectively. The dielectric constant $\epsilon_r = 8$ is for BLG and $\epsilon_r = 16$ is for TriLG.

In Supplementary Figure 3, we present the ground states of TriLG at integer filling factors $\nu = 1$ (a) and $\nu = 2$ (b), obtained using the band-projected HF method. These ground states correspond to topological correlated insulators stabilized by spontaneous symmetry breaking: At $\nu = 1$, the system realizes a spin- and valley-polarized Chern insulator with Chern number $|C| = 1$. In contrast, at $\nu = 2$, the ground state remains spin-degenerate but becomes valley-polarized, yielding a Chern insulator with $|C| = 2$.

FULL-BAND HARTREE-FOCK METHOD

We now go beyond the ‘‘Born-Oppenheimer-type’’ treatment and turn to the full-band Hartree-Fock (HF) method, which treats electrons transferred to the substrate and within the RMG on an equal footing. Technically, the full-band HF method is unavoidable when treating band dispersions with substantially different energy scales, as in our case. In particular, no physically sensible band cutoff exists for a band-projected HF calculation, which again necessitates a full-band HF treatment.

Low-energy electrons within RMG are described by the standard non-interacting $\mathbf{k} \cdot \mathbf{p}$ model, while the electrons transferred to the substrate are modeled as a two-dimensional electron gas with a parabolic band dispersion. Owing



Supplementary Figure 3. Energy band structure for HF ground state of TriLG at filling factor $\nu = 1$ (a) with $E_{\text{ext}} = -0.20 \text{ V/nm}$ and $n_{\text{tot}} = 2.63 \times 10^{12} \text{ cm}^{-2}$, at filling factor $\nu = 2$ (b) with $E_{\text{ext}} = -0.20625 \text{ V/nm}$ and $n_{\text{tot}} = 2.76 \times 10^{12} \text{ cm}^{-2}$.

to the large interlayer separation d_0 and lattice mismatch, direct interlayer electron hopping is negligible; however, long-range Coulomb interactions between the two subsystems remain significant. We introduce a layer-dependent Coulomb potential to distinguish the interlayer interactions and intralayer interactions. The total Hamiltonian of the coupled RMG-insulator substrate heterostructure is expressed as:

$$\hat{H}^0 = \sum_{\lambda\lambda',\sigma\mathbf{k}} \epsilon_{\lambda,\lambda'}^\sigma(\mathbf{k}) \hat{c}_{\lambda\sigma}^\dagger(\mathbf{k}) \hat{c}_{\lambda'\sigma}(\mathbf{k}), \quad (\text{S40a})$$

$$\hat{H}_{\text{int}} = \frac{1}{2N_s} \sum_{\sigma\sigma'} \sum_{\mathbf{k}\mathbf{k}'\mathbf{q}} V_{\lambda,\lambda'}(\mathbf{q}) \times \hat{c}_{\lambda\sigma}^\dagger(\mathbf{k} + \mathbf{q}) \hat{c}_{\lambda'\sigma'}^\dagger(\mathbf{k}' - \mathbf{q}) \hat{c}_{\lambda'\sigma'}(\mathbf{k}') \hat{c}_{\lambda\sigma}(\mathbf{k}),$$

where the composite index $\lambda \equiv (\mu, l, \alpha)$ collectively labels the valley, layer, and sublattice degrees of freedom, and σ denotes the spin index. We consider the 2D electron gas on the substrate's side with a locked valley-layer-sublattice degree of freedom. Accordingly, $\lambda = -1$ is assigned to the surface of the substrate, and non-negative values $\lambda \geq 0$ correspond to graphene layers of the RMG. Taking the BLG-substrate heterostructure with two-sublattice and two-valley degrees of freedom as an example, the relation $\lambda = 4\mu + 2l + \alpha$ establishes the correspondence between an electron with index λ and an electron residing in layer l , valley μ , and sublattice α . The operator $\hat{c}_{\lambda\sigma}^\dagger(\mathbf{k})$ ($\hat{c}_{\lambda\sigma}(\mathbf{k})$) creates (annihilates) an electron with wave vector \mathbf{k} expanded around the CBM of the substrate or the CNP of RMG, carrying the composite index λ and spin σ . Again taking the BLG-based charge transfer heterostructure as an example, the expression of the non-interacting kinetic term $\epsilon_{\lambda\lambda',\sigma\mathbf{k}}$ is :

$$\epsilon_{\sigma\mathbf{k}} = \begin{pmatrix} \frac{\hbar^2 k^2}{2m^*} + E_{\text{CBM}} & 0 & 0 & 0 & 0 \\ 0 & h_{\text{intra}}^{0,+} & (h_{\text{inter}}^{0,+})^\dagger & 0 & 0 \\ 0 & h_{\text{inter}}^{0,+} & h_{\text{intra}}^{0,+} & 0 & 0 \\ 0 & 0 & 0 & h_{\text{intra}}^{0,-} & (h_{\text{inter}}^{0,-})^\dagger \\ 0 & 0 & 0 & h_{\text{inter}}^{0,-} & h_{\text{intra}}^{0,-} \end{pmatrix}. \quad (\text{S41})$$

The effective mass m^* and E_{CBM} , the initial energy of the CBM of substrate relative to the CNP of RMG, are set to be tunable parameters in this section. The interaction Hamiltonian \hat{H}_{int} not only contains the e-e Coulomb interaction between electrons on graphene side, but also interactions between electrons in the substrate and coupling between them. As discussed previously, we adopted a layer-dependent screened Coulomb potential $V_{ll'}(\mathbf{q})$ Eq. (S34) to distinguish the difference between intralayer Coulomb interaction and interlayer Coulomb interaction. In our numerical calculations, We begin with trial initial states in which translational symmetry is weakly broken by introducing a trial superlattice potential, whose lattice constant is determined by $\sqrt{3}L_s^2 n_{\text{sub}}/2 = 2$, and then perform self-consistent Hartree-Fock iterations until convergence is reached. N_s is the number of the unit cell in the system. Hence, wave vectors are folded into the corresponding mini Brillouin zone by $\mathbf{k} = \tilde{\mathbf{k}} + \mathbf{G}$ and $\mathbf{q} = \tilde{\mathbf{q}} + \mathbf{Q}$. \mathbf{G} and \mathbf{Q} are reciprocal lattice vectors of mini Brillouin zone. Due to exponentially decaying potential, we only consider the dominant intravalley interaction. Applying Hartree-Fock approximation to the full band interaction Hamiltonian, we get:

$$\hat{V}_H^{full} = \frac{1}{N_s} \sum_{\sigma\sigma'} \sum_{\tilde{\mathbf{k}}\tilde{\mathbf{k}'}} \sum_{\mathbf{G}, \mathbf{G}', \mathbf{Q}} V_{\lambda\lambda'}(\mathbf{Q}) \left\langle \hat{c}_{\sigma'\lambda'\mathbf{G}'-\mathbf{Q}, \tilde{\mathbf{k}}}^\dagger \hat{c}_{\sigma'\lambda'\mathbf{G}', \tilde{\mathbf{k}'}} \right\rangle \hat{c}_{\sigma\lambda\mathbf{G}+\mathbf{Q}, \tilde{\mathbf{k}}}^\dagger \hat{c}_{\sigma\lambda\mathbf{G}, \tilde{\mathbf{k}}} \quad (S42)$$

$$\hat{V}_F^{full} = -\frac{1}{N_s} \sum_{\sigma\sigma'} \sum_{\tilde{\mathbf{k}}\tilde{\mathbf{k}'}} \sum_{\mathbf{G}, \mathbf{G}', \mathbf{Q}} V_{\lambda\lambda'}(\tilde{\mathbf{k}}' - \tilde{\mathbf{k}} + \mathbf{G}' - \mathbf{G} + \mathbf{Q}) \times \left\langle \hat{c}_{\sigma\lambda\mathbf{G}'+\mathbf{Q}, \tilde{\mathbf{k}}}^\dagger \hat{c}_{\sigma'\lambda'\mathbf{G}', \tilde{\mathbf{k}'}} \right\rangle \hat{c}_{\sigma'\lambda'\mathbf{G}-\mathbf{Q}, \tilde{\mathbf{k}}}^\dagger \hat{c}_{\sigma\lambda\mathbf{G}, \tilde{\mathbf{k}}} \quad (S43)$$

REFERENCES

[†] lvxin@shanghaitech.edu.cn
[‡] liujp@shanghaitech.edu.cn

[1] A. K. Geim and I. V. Grigorieva, *Nature* **499**, 419 (2013).
[2] H. Zhou, T. Xie, A. Ghazaryan, T. Holder, J. R. Ehrets, E. M. Spanton, T. Taniguchi, K. Watanabe, E. Berg, M. Serbyn, et al., *Nature* **598**, 429 (2021).
[3] Q. Tong, F. Liu, J. Xiao, and W. Yao, *Nano Letters* **18**, 7194 (2018).
[4] X. Huang, T. Wang, S. Miao, C. Wang, Z. Li, Z. Lian, T. Taniguchi, K. Watanabe, S. Okamoto, D. Xiao, S.-F. Shi, and Y.-T. Cui, *Nature Physics* **17**, 715 (2021).
[5] G. Chen, A. L. Sharpe, E. J. Fox, Y.-H. Zhang, S. Wang, L. Jiang, B. Lyu, H. Li, K. Watanabe, T. Taniguchi, Z. Shi, T. Senthil, D. Goldhaber-Gordon, Y. Zhang, and F. Wang, *Nature* **579**, 56 (2020).
[6] J. Xie, Z. Huo, X. Lu, Z. Feng, Z. Zhang, W. Wang, Q. Yang, K. Watanabe, T. Taniguchi, K. Liu, Z. Song, X. C. Xie, J. Liu, and X. Lu, Tunable fractional chern insulators in rhombohedral graphene superlattices (2025), arXiv:2405.16944 [cond-mat.mes-hall].
[7] Y. Choi, Y. Choi, M. Valentini, C. L. Patterson, L. F. W. Holleis, O. I. Sheekey, H. Stoyanov, X. Cheng, T. Taniguchi, K. Watanabe, and A. F. Young, *Nature* **639**, 342–347 (2025).
[8] D. Waters, A. Okounkova, R. Su, B. Zhou, J. Yao, K. Watanabe, T. Taniguchi, X. Xu, Y.-H. Zhang, J. Folk, and M. Yankowitz, *Physical Review X* **15**, 10.1103/physrevx.15.011045 (2025).
[9] H. Xiang, J. Ding, J. Hua, N. Liu, W. Zhou, Q. Chen, K. Watanabe, T. Taniguchi, N. Xin, W. Zhu, and S. Xu, Continuously tunable anomalous hall crystals in rhombohedral heptalayer graphene (2025), arXiv:2502.18031 [cond-mat.mes-hall].
[10] Z. Lu, T. Han, Y. Yao, Z. Hadjri, J. Yang, J. Seo, L. Shi, S. Ye, K. Watanabe, T. Taniguchi, and L. Ju, *Nature* **637**, 1090 (2025).
[11] S. H. Aronson, T. Han, Z. Lu, Y. Yao, J. P. Butler, K. Watanabe, T. Taniguchi, L. Ju, and R. C. Ashoori, *Physical Review X* **15**, 10.1103/75gl-jzl6 (2025).
[12] W. Zhou, J. Ding, J. Hua, L. Zhang, K. Watanabe, T. Taniguchi, W. Zhu, and S. Xu, *Nature Communications* **15**, 2597 (2024).
[13] X. Han, Q. Liu, Y. Wang, R. Niu, Z. Qu, Z. Wang, Z. Li, C. Han, K. Watanabe, T. Taniguchi, Z. Song, J. Liu, J. Mao, Z. Han, B. L. Chittari, J. Jung, Z. Gan, and J. Lu, *Nano Letters* **24**, 6286 (2024).
[14] J. Ding, H. Xiang, J. Hua, W. Zhou, N. Liu, L. Zhang, N. Xin, B. Wu, K. Watanabe, T. Taniguchi, Z. Sofer, W. Zhu, and S. Xu, *Physical Review X* **15**, 10.1103/physrevx.15.011052 (2025).
[15] J. Zheng, S. Wu, K. Liu, B. Lyu, S. Liu, Y. Sha, Z. Li, K. Watanabe, T. Taniguchi, J. Jia, Z. Shi, and G. Chen, Switchable chern insulator, isospin competitions and charge density waves in rhombohedral graphene moire superlattices (2024), arXiv:2412.09985 [cond-mat.str-el].
[16] Z. Wang, Q. Liu, X. Han, Z. Li, W. Zhao, Z. Qu, C. Han, K. Watanabe, T. Taniguchi, Z. V. Han, S. Zhou, B. Tong, G. Liu, L. Lu, J. Liu, F. Wu, and J. Lu, Electrical switching of chern insulators in moire rhombohedral heptalayer graphene (2025), arXiv:2503.00837 [cond-mat.mes-hall].
[17] E. C. Regan, D. Wang, C. Jin, M. I. Bakti Utama, B. Gao, X. Wei, S. Zhao, W. Zhao, Z. Zhang, K. Yumigeta, M. Blei, J. D. Carlström, K. Watanabe, T. Taniguchi, S. Tongay, M. Crommie, A. Zettl, and F. Wang, *Nature* **579**, 359 (2020).
[18] Y. Tang, L. Li, T. Li, Y. Xu, S. Liu, K. Barmak, K. Watanabe, T. Taniguchi, A. H. MacDonald, J. Shan, and K. F. Mak, *Nature* **579**, 353 (2020).
[19] Y. Xu, S. Liu, D. A. Rhodes, K. Watanabe, T. Taniguchi, J. Hone, V. Elser, K. F. Mak, and J. Shan, *Nature* **587**, 214 (2020).
[20] X. Lu, S. Zhang, Y. Wang, X. Gao, K. Yang, Z. Guo, Y. Gao, Y. Ye, Z. Han, and J. Liu, *Nature Communications* **14**, 5550 (2023).
[21] Y. Wang, X. Gao, K. Yang, P. Gu, X. Lu, S. Zhang, Y. Gao, N. Ren, B. Dong, Y. Jiang, K. Watanabe, T. Taniguchi, J. Kang, W. Lou, J. Mao, J. Liu, Y. Ye, Z. Han, K. Chang, J. Zhang, and Z. Zhang, *Nature Nanotechnology* **17**, 1272 (2022).
[22] K. Yang, X. Gao, Y. Wang, T. Zhang, Y. Gao, X. Lu, S. Zhang, J. Liu, P. Gu, Z. Luo, R. Zheng, S. Cao, H. Wang, X. Sun, K. Watanabe, T. Taniguchi, X. Li, J. Zhang, X. Dai, J.-H. Chen, Y. Ye, and Z. Han, *Nature Communications* **14**, 2136 (2023).
[23] Y. Guo, J. Li, X. Zhan, C. Wang, M. Li, B. Zhang, Z. Wang, Y. Liu, K. Yang, H. Wang, W. Li, P. Gu, Z. Luo, Y. Liu, P. Liu, B. Chen, K. Watanabe, T. Taniguchi, X.-Q. Chen, C. Qin, J. Chen, D. Sun, J. Zhang, R. Wang, J. Liu, Y. Ye, X. Li, Y. Hou, W. Zhou, H. Wang, and Z. Han, *Nature* **630**, 346 (2024).
[24] E. Wigner, *Phys. Rev.* **46**, 1002 (1934).

[25] E. Y. Andrei, D. K. Efetov, P. Jarillo-Herrero, A. H. MacDonald, K. F. Mak, T. Senthil, E. Tutuc, A. Yazdani, and A. F. Young, *Nature Reviews Materials* **6**, 201 (2021).

[26] R. Bistritzer and A. H. MacDonald, *Proceedings of the National Academy of Sciences* **108**, 12233 (2011), <https://www.pnas.org/doi/pdf/10.1073/pnas.1108174108>.

[27] G. Tenasini, D. Soler-Delgado, Z. Wang, F. Yao, D. Dumcenco, E. Giannini, K. Watanabe, T. Taniguchi, C. Moultsdale, A. Garcia-Ruiz, V. I. Fal'ko, I. Gutiérrez-Lezama, and A. F. Morpurgo, *Nano Letters* **22**, 6760 (2022), pMID: 35930625.

[28] C.-C. Tseng, T. Song, Q. Jiang, Z. Lin, C. Wang, J. Suh, K. Watanabe, T. Taniguchi, M. A. McGuire, D. Xiao, J.-H. Chu, D. H. Cobden, X. Xu, and M. Yankowitz, *Nano Letters* **22**, 8495 (2022).

[29] N. Tilak, M. Altvater, S.-H. Hung, C.-J. Won, G. Li, T. Kaleem, S.-W. Cheong, C.-H. Chung, H.-T. Jeng, and E. Y. Andrei, *Nature Communications* **15**, 8056 (2024).

[30] H. Zhou, T. Xie, T. Taniguchi, K. Watanabe, and A. F. Young, *Nature* **598**, 434 (2021).

[31] Y. Shi, S. Xu, Y. Yang, S. Slizovskiy, S. V. Morozov, S.-K. Son, S. Ozdemir, C. Mullan, J. Barrier, J. Yin, A. I. Berdyugin, B. A. Piot, T. Taniguchi, K. Watanabe, V. I. Fal'ko, K. S. Novoselov, A. K. Geim, and A. Mishchenko, *Nature* **584**, 210 (2020).

[32] K. Myhro, S. Che, Y. Shi, Y. Lee, K. Thilahar, K. Bleich, D. Smirnov, and C. N. Lau, *2D Materials* **5**, 045013 (2018).

[33] T. Han, Z. Lu, G. Scuri, J. Sung, J. Wang, T. Han, K. Watanabe, T. Taniguchi, L. Fu, H. Park, and L. Ju, *Nature* **623**, 41 (2023).

[34] T. Han, Z. Lu, G. Scuri, J. Sung, J. Wang, T. Han, K. Watanabe, T. Taniguchi, H. Park, and L. Ju, *Nat. Nanotechnol.* **19**, 181 (2024).

[35] T. Han, Z. Lu, Y. Yao, J. Yang, J. Seo, C. Yoon, K. Watanabe, T. Taniguchi, L. Fu, F. Zhang, and L. Ju, *Science* **384**, 647 (2024), <https://www.science.org/doi/pdf/10.1126/science.adk9749>.

[36] Y. Sha, J. Zheng, K. Liu, H. Du, K. Watanabe, T. Taniguchi, J. Jia, Z. Shi, R. Zhong, and G. Chen, *Science* **384**, 414 (2024), <https://www.science.org/doi/pdf/10.1126/science.adj8272>.

[37] T. Han, Z. Lu, Z. Hadjri, L. Shi, Z. Wu, W. Xu, Y. Yao, A. A. Cotten, O. Sharifi Sedeh, H. Weldeyesus, J. Yang, J. Seo, S. Ye, M. Zhou, H. Liu, G. Shi, Z. Hua, K. Watanabe, T. Taniguchi, P. Xiong, D. M. Zumbühl, L. Fu, and L. Ju, *Nature* **643**, 654 (2025).

[38] C. L. Patterson, O. I. Sheekey, T. B. Arp, L. F. W. Holleis, J. M. Koh, Y. Choi, T. Xie, S. Xu, E. Redekop, G. Babikyan, H. Zhou, X. Cheng, T. Taniguchi, K. Watanabe, C. Jin, E. Lantagne-Hurtubise, J. Alicea, and A. F. Young, *Superconductivity and spin canting in spin-orbit proximitized rhombohedral trilayer graphene* (2024), arXiv:2408.10190 [cond-mat.mes-hall].

[39] J. Yang, X. Shi, S. Ye, C. Yoon, Z. Lu, V. Kakani, T. Han, J. Seo, L. Shi, K. Watanabe, T. Taniguchi, F. Zhang, and L. Ju, *Impact of spin-orbit coupling on superconductivity in rhombohedral graphene* (2025), arXiv:2408.09906 [cond-mat.supr-con].

[40] K. Liu, J. Zheng, Y. Sha, B. Lyu, F. Li, Y. Park, Y. Ren, K. Watanabe, T. Taniguchi, J. Jia, W. Luo, Z. Shi, J. Jung, and G. Chen, *Nature Nanotechnology* **19**, 188 (2024).

[41] Y. Zhang, Y.-Y. Zhou, S. Zhang, H. Cai, L.-H. Tong, W.-Y. Liao, R.-J. Zou, S.-M. Xue, Y. Tian, T. Chen, Q. Tian, C. Zhang, Y. Wang, X. Zou, X. Liu, Y. Hu, Y.-N. Ren, L. Zhang, L. Zhang, W.-X. Wang, L. He, L. Liao, Z. Qin, and L.-J. Yin, *Nature Nanotechnology* **20**, 222 (2025).

[42] H. Zhang, Q. Li, M. G. Scheer, R. Wang, C. Tuo, N. Zou, W. Chen, J. Li, X. Cai, C. Bao, M.-R. Li, K. Deng, K. Watanabe, T. Taniguchi, M. Ye, P. Tang, Y. Xu, P. Yu, J. Avila, P. Dudin, J. D. Denlinger, H. Yao, B. Lian, W. Duan, and S. Zhou, *Proceedings of the National Academy of Sciences* **121**, e2410714121 (2024).

[43] Z. Guo and J. Liu, *Nature Communications* **16**, 11289 (2025).

[44] B. A. Bernevig and Y. H. Kwan, "berry trashcan" model of interacting electrons in rhombohedral graphene (2025), arXiv:2503.09692 [cond-mat.str-el].

[45] S. A. A. Ghorashi, A. Dunbrack, A. Abouelkomsan, J. Sun, X. Du, and J. Cano, *Phys. Rev. Lett.* **130**, 196201 (2023).

[46] S. A. A. Ghorashi and J. Cano, *Phys. Rev. B* **107**, 195423 (2023).

[47] S. Wang, Z. Zhan, X. Fan, Y. Li, P. A. Pantaleón, C. Ye, Z. He, L. Wei, L. Li, F. Guinea, S. Yuan, and C. Zeng, *Phys. Rev. Lett.* **133**, 066302 (2024).

[48] Y. Zeng, T. M. R. Wolf, C. Huang, N. Wei, S. A. A. Ghorashi, A. H. MacDonald, and J. Cano, *Phys. Rev. B* **109**, 195406 (2024).

[49] Z. Zhan, Y. Li, and P. A. Pantaleón, *Phys. Rev. B* **111**, 045148 (2025).

[50] Y. Shi, B. Xie, F. Ren, X. Cai, Z. Guo, Q. Li, X. Lu, N. Regnault, Z. Liu, and J. Liu, *Phys. Rev. Lett.* **135**, 256603 (2025).

[51] X. Zhu, P. B. Littlewood, M. S. Hybertsen, and T. M. Rice, *Phys. Rev. Lett.* **74**, 1633 (1995).

[52] D. I. Pikulin and T. Hyart, *Phys. Rev. Lett.* **112**, 176403 (2014).

[53] Q. Zhu, M. W.-Y. Tu, Q. Tong, and W. Yao, *Science Advances* **5**, eaau6120 (2019).

[54] B. Seradjeh, J. E. Moore, and M. Franz, *Phys. Rev. Lett.* **103**, 066402 (2009).

[55] Y. Shao and X. Dai, *Phys. Rev. B* **109**, 155107 (2024).

[56] J. Zhu and S. Das Sarma, *Phys. Rev. B* **109**, 085129 (2024).

[57] J. Zhu and S. Das Sarma, *Phys. Rev. B* **112**, 214521 (2025).

[58] Y. Zeng and A. H. MacDonald, *Phys. Rev. B* **102**, 085154 (2020).

[59] See Supplemental Materials for details on: (i) $\mathbf{k} \cdot \mathbf{p}$ model of rhombohedral multilayer graphene; (ii) Fock self energy correction and (iii) self-consistent screening method incorporating charge transfer; (iv) continuum model describing rhombohedral multilayer graphene coupled to insulating substrate via interlayer Coulomb coupling; (v) renormalization of the continuum model parameters due to interactions with remote-band electrons (vi) band-projected Hartree-Fock formalism

and band structures of correlated Chern insulator states for TriLG; (vii) full-band Hartree-Fock method.

[60] N. D. Drummond and R. J. Needs, Phys. Rev. Lett. **102**, 126402 (2009).

[61] J. Gonzalez, F. Guinea, and V. M. A. H., Nuclear Physics B **424**, 595 (1994).

[62] O. Vafek and J. Kang, Phys. Rev. Lett. **125**, 257602 (2020).

[63] Z. Guo, X. Lu, B. Xie, and J. Liu, Phys. Rev. B **110**, 075109 (2024).

[64] P. Moon and M. Koshino, Physical Review B **87**, 205404 (2013).

[65] P. Moon and M. Koshino, Phys. Rev. B **90**, 155406 (2014).

[66] N. D. Drummond and R. J. Needs, Phys. Rev. Lett. **102**, 126402 (2009).

[67] F. Rapisarda and G. Senatore, Aust. J. Phys. **49**, 161–182 (1994).

[68] Y. Jang, Y. Park, J. Jung, and H. Min, Phys. Rev. B **108**, L041101 (2023).

[69] E. McCann, Phys. Rev. B **74**, 161403 (2006).

[70] A. A. Avetisyan, B. Partoens, and F. M. Peeters, Phys. Rev. B **79**, 035421 (2009).

[71] A. A. Avetisyan, B. Partoens, and F. M. Peeters, Phys. Rev. B **80**, 195401 (2009).

[72] M. Koshino and E. McCann, Phys. Rev. B **79**, 125443 (2009).

[73] Z. Guo, X. Lu, B. Xie, and J. Liu, Phys. Rev. B **110**, 075109 (2024).

[74] D. C. Elias, R. Gorbachev, A. Mayorov, S. Morozov, A. Zhukov, P. Blake, L. Ponomarenko, I. Grigorieva, K. Novoselov, F. Guinea, et al., Nature Physics **7**, 701 (2011).

[75] O. Vafek and J. Kang, Phys. Rev. Lett. **125**, 257602 (2020).

[76] S. Zhang, X. Dai, and J. Liu, Phys. Rev. Lett. **128**, 026403 (2022).